International Journal of Non-Linear Mechanics 118 (2020) 103298

Contents lists available at ScienceDirect

International Journal of Non-Linear Mechanics

journal homepage: www.elsevier.com/locate/nlm

Electrostatic arch micro-tweezers

Ayman M. Alneamy [a,b,*], Mahmoud E. Khater [c], Ahmed K. Abdel-Aziz [d], Glenn R. Heppler [a], Eihab M. Abdel-Rahman [a]

[a] Department of Systems Design Engineering, University of Waterloo, Waterloo, On, Canada
[b] Department of Mechanical Engineering, Jazan University, Jazan, Saudi Arabia
[c] Department of Mechanical Engineering, KFUPM, Dhahran, Saudi Arabia
[d] Department of Electrical and Computer Engineering, University of Waterloo, Waterloo, On, Canada

ARTICLE INFO

Keywords:
Arch beam
Snap-through
Tweezers
Rotary inertia

ABSTRACT

This paper presents a novel electrostatic micro-tweezers to manipulate particles with diameters up to 14 μm. The tweezers consist of two grip-arms mounted to an electrostatically actuated initially curved micro-beam. It exploits bistable equilibria, resulting from a snap-through instability, to close the separation distance between the two arms allowing them to grasp a large range of objects. The tweezers offer further control beyond the snap-through point, via electrostatic actuation, to increase pressure on larger objects or grasp smaller objects. The tweezers are fabricated in a p-type Silicon on Insulator (SOI) wafer. Euler-Bernoulli beam theory is utilized to derive the governing equation of motion taking into account the arms' rotary inertia and the electrostatic fringing field. A reduced-order model (ROM) is developed utilizing two, three and five symmetric modes in a Galerkin expansion. A finite element model (FEM) is also developed to validate the ROM and to study the arm tips' separation as a function of actuation voltage. The five-mode ROM is found to be convergent and accurate except in the vicinity of the snap-through saddle-node bifurcation. Our analysis shows that the tweezers can manipulate micro-particles with diameters ranging from 5 to 12 μm with an operating voltage range limited by the snap-back voltage 100.2 V and the pull-in voltage 153.2 V.

1. Introduction

A present need exists for the development of Micro-Device-Assembly (MDA) systems [1]. In addition, the complexity of micro-particle geometries, their internal microstructure and varying material properties, have led many researchers to develop MEMS devices to precisely locate and manipulate objects such as DNA strands and white and red blood cells [2]. These devices provide a bridge between the macro systems and a tiny world that is only visible under microscopes and with advanced tools. Automatically handling and manipulating those particles requires consideration of device compatibility, size, integration with electronics, resolution, power consumption and design configuration. Micro-tweezers are the typical end-effectors deployed to handle micro-particles.

The actuation mechanisms for micro-tweezers fall into four categories: electromagnetic, piezoelectric, electrothermal and electrostatic. Electromagnetic micro-tweezers are larger in size and output force but harder to fabricate [3]. Piezoelectric tweezers have a smaller stroke which restricts their use [4]. Electrothermal tweezers are often preferred due to their simplicity of their fabrication. They also require a small voltage and produce a large grip force [5]. However, they are limited to applications where heat dissipation from the actuator does not damage sensitive targets such as biological cells. Because of these limitations, many researchers have turned their attention to electrostatic actuation of MEMS tweezers due to many inherent advantages compared to the electrothermal actuation, including lower power consumption, controllability over the travel distance and simpler fabrication processes.

Electrostatic MEMS tweezers have been designed with a wide variety of gripping mechanisms but only two actuation schemes: parallel-plate and interdigitated comb-fingers. The tweezers designed by Varona *et al.* [6] and Chang *et al.* [7] presented the only parallel-plate actuation schemes reported to date. Their designs reduces the micro-tweezers size, however they requires more than 45 V to close a gap of 2 μm and 93 V to close a gap of 1.2 μm, respectively. Micro-tweezers based on interdigitated comb-finger drives have been more popular with efforts devoted to increase the gripping range and reducing the actuation voltage.

Many researchers [8–13] utilized flexible beams to convert the linear motion of comb-finger actuators to rotational gripper arms motion. The maximum arm stroke and actuation voltage they realized in each case are listed in Table 1. On the other hand, Chen *et al.* [14] used linear comb-fingers to directly close the grip arms and achieve a stroke

* Corresponding author at: Department of Systems Design Engineering, University of Waterloo, Waterloo, On, Canada.
E-mail address: aalneamy@uwaterloo.ca (A.M. Alneamy).

https://doi.org/10.1016/j.ijnonlinmec.2019.103298
Received 4 April 2019; Received in revised form 2 August 2019; Accepted 30 September 2019
Available online 3 October 2019
0020-7462/© 2019 Elsevier Ltd. All rights reserved.

Table 1
Relevant works on electrostatic micro-tweezers.

Actuator	Stroke (μm)	Voltage (V)
Parallel-plate		
Varona et al. [6]	2	45
Chang et al. [7]	1.2	93
Linear comb-fingers		
Volland et al. [8]	20	80
Beyeler et al. [9]	100	150
Chen et al. [10]	25	80
Bazaz et al. [11]	17	50
Hamedi et al. [12]	26	82
Xu [13]	63	72
Chen et al. [14]	7.5	50
Demaghsi et al. [15]	12	55
Rotary comb-fingers		
Chang et al. [16]	94	100
Piriyanont et al. [17]	85	80

of 7.5 μm at voltage of 50 V. Micro-tweezers have also demonstrated the ability to hold objects under a static load (DC voltage) and to release dynamically under AC signal [15]. Other researchers [16,17] have recently employed rotary comb-fingers to directly actuate the tweezers arms, thereby drastically increasing arms without increasing the actuation voltage as can be seen in Table 1.

Most electrostatic micro-tweezers use comb-finger actuator which guarantees them a larger stroke at the expense of a larger footprint. To date, the use of more compact parallel-plate actuators has been hampered by the small stroke imposed by the pull-in instability. We propose to reduce the footprint of micro-tweezers while increasing their stroke by using parallel-plate curved beams (arches) as an actuation platform. These actuators can switch from one stable equilibrium to another resulting in a larger stroke. The transition between the two stable equilibria is commonly referred to as snap-through.

Curved micro-beam actuators can be realized by buckling initially straight beams through compressive axial loads or can be fabricated in an initially curved. The latter type has been used in a variety of applications, such as switches, filters and mechanical memories [18–20].

In this paper, we present a novel electrostatic micro-tweezers based on bistable micro-actuators. We also develop analytical and FEM models of the micro-tweezers taking into the account the arm's inertia and the electrostatic fringing field. Finally, we use the model to investigate the micro-tweezers operational range and capabilities to manipulate micro-particles.

2. Design and fabrication

The electrostatic micro-tweezers consist of an initially curved beam with two arms mounted to it and a side electrode, Fig. 1. The distance between the beam anchors (center line) is $\ell_b = 1000\,\mu m$. The beam thickness and initial mid-point rise are $h_b = 3\,\mu m$ and $h_\circ = 3.5\,\mu m$, respectively. The initial capacitor gap between the side electrode and the center line is $d = 11\,\mu m$, Fig. 2 (b). The arms' length and a thickness are $\ell_a = 250\,\mu m$ and $h_a = 4\,\mu m$, respectively. The beam and arms are fabricated into a structural layer with a thickness of $b = 30\,\mu m$. The distance between the arms attachment points along the center line is 300 μm. The arms' are fabricated at an angle of 55.11° with respect to the cord length resulting in an initial tip distance of 14 μm, Fig. 2 (c).

The tweezers were fabricated using a p-type < 100 > low resistivity Silicon on Insulator (SOI) wafer. The structural layer thickness is 30 ± 3 μm, the buried oxide layer thickness is 1 μm and the handle layer thickness is 550 μm. The material properties of the single-crystal silicon layer are listed in Table 2. A cross-section for the final fabrication step is shown in Fig. 2 (a). SEM pictures of the fabricated device before the backside etch and release process are shown in Fig. 2 (b) and (c).

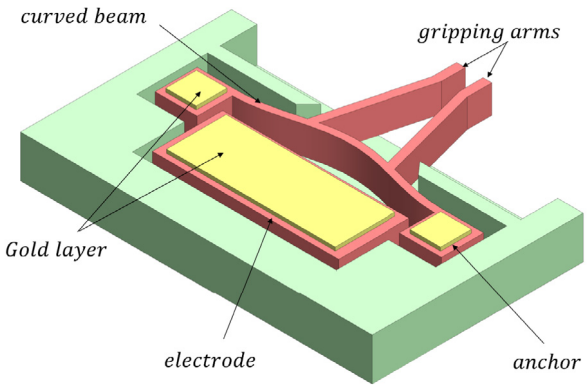

Fig. 1. A 3D drawing of the arch micro-tweezers.

(a)

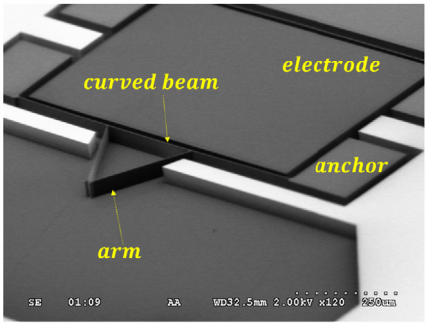

(b)

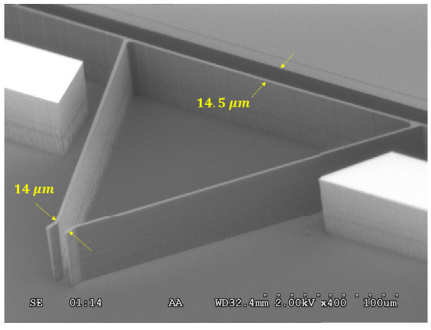

(c)

Fig. 2. (a) A cross-section of the last fabrication step, (b) an SEM picture of the fabricated device and (c) a close-up SEM picture on the grip arms.

3. Tweezers model

To derive the equation of motion describing the transverse response and the associated boundary and initial conditions of the electrostatic

Table 2
Material properties of the used SOI wafer.

Description	Value
Density (ρ)	2330 kg/m^3
Young's Modulus (E)	129 GPa
Yield strength (σ_y)	1.2 GPa
Poisson's ratio (ν)	0.22

micro-tweezers, Fig. 2 (a), we utilize Euler-Bernoulli beam theory. Then, we assume that the tweezers arms are rigid bodies and their elastic deformations is ignored. The tweezers is composed of an arch micro-beam with a cross-sectional area of A_b and an area moment of inertia of I_b carrying two identical arms A_1 and A_2 with equal masses m_a and mass moments of inertia J_a located at distances ℓ_1 and ℓ_2 from the origin as shown in Fig. 3.

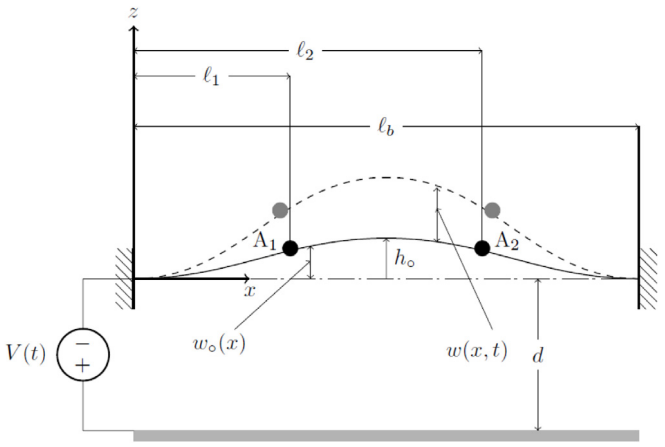

Fig. 3. A schematic of the arch beam carrying two masses.

The beam is assumed uniform and isotropic. The initial shape of the micro-beam was laid out to follow the expression

$$w_\circ(x) = \frac{h_\circ}{2}[1 - \cos(\frac{2\pi x}{\ell_b})] \tag{1}$$

Following [21,22] in the derivation of the equation of motion, we consider a differential beam element initially dx long. Its left edge P is located at $(x, w_\circ)$, see Fig. 4. After the deformation, the left edge moves to P* at

$$x^* = x + u \quad , \quad z^* = w + w_\circ \tag{2}$$

where u is the displacement along x-axis and w is the transverse displacement along z-axis measured from $w_\circ$. Therefore, the deformed element length can be calculated as

$$ds = \sqrt{(dx^*)^2 + (dz^*)^2} \tag{3}$$

Then, differentiating x^* and z^* with respect to x yields

$$dx^* = (1 + u')\,dx \quad , \quad dz^* = (w' + w'_\circ)\,dx \tag{4}$$

substituting Eq. (4) into Eq. (3) gives

$$ds = \sqrt{(1 + u')^2 + (w' + w'_\circ)^2}\; dx \tag{5}$$

Assuming a small initial rise $h_\circ << \ell_b$, Eq. (5) can be simplified to

$$\lambda = \frac{ds}{dx} = \sqrt{1 + 2u' + u'^2 + w'^2 + 2w'_\circ w'} \tag{6}$$

The axial strain of the beam element is given by

$$\epsilon_{xx} = \frac{ds - dx}{dx} \tag{7}$$

Scaling the transverse displacement $w(x)$ and initial shape $w_\circ(x)$ at order O(ϵ^1), the axial displacement at order O(ϵ^2) and the other system

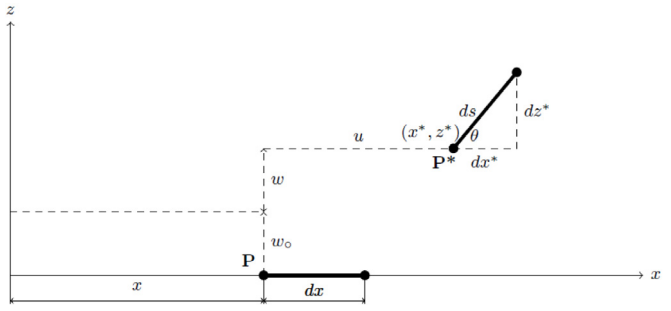

Fig. 4. A segment of the curved beam showing the location before **P** and after deformation **P***.

Table 3
Scales of the beam parameters.

Parameter	Scaling order O(ϵ^n)
w	$O(\epsilon^1)$
u	$O(\epsilon^2)$
$\dot{w}', \dot{w}'', \ddot{w}', \ddot{w}''$	$O(\epsilon^1)$
$\dot{u}$	$O(\epsilon^3)$
ü	$O(\epsilon^4)$
ℓ, b, d	$O(\epsilon^0)$
h	$O(\epsilon^1)$
A	$O(\epsilon^1)$
I	$O(\epsilon^3)$
J	$O(\epsilon^1)$

parameters scaling properties as listed in Table Table 3. Expanding ϵ_{xx} in Taylor series and retaining terms up to order O(ϵ^3), we can write

$$\epsilon_{xx} = u' + w'_\circ w' + \frac{1}{2}w'^2 \tag{8}$$

This formula describes the element elongation for the small strains and moderate rotations [22]. Recalling that for Euler-Bernoulli beam, the axial and transverse displacements can be written as

$$u = \bar{u} - \zeta \bar{w}' \quad , \quad w = \bar{w} \tag{9}$$

where the bar represents the displacement of the reference axis in both directions and ζ is a coordinate pointing into the curvature. Substituting this equation into Eq. (8), the total strain of the initially curved beam can be written up to order O(ϵ^3) as

$$\epsilon_{xx} = \bar{u}' - \zeta \bar{w}'' + w'_\circ \bar{w}' + \frac{1}{2}\bar{w}'^2 \tag{10}$$

The beam element rotation angle θ can be expressed as

$$\sin\theta = \frac{dz^*}{ds} = \frac{w'_\circ + w'}{\lambda} \tag{11}$$

$$\cos\theta = \frac{dx^*}{ds} = \frac{1 + u'}{\lambda} \tag{12}$$

differentiating Eq. (11) and Eq. (12) with respect to the time t yields

$$\dot{\theta}\cos\theta = \frac{(1 + u')[(1 + u')\dot{w}' - (w'_\circ + w')\dot{u}']}{(1 + 2u' + u'^2 + w'^2 + 2w'_\circ w')^{\frac{3}{2}}} \tag{13}$$

and using Eq. (12) in Eq. (13), we obtain

$$\dot{\theta} = \frac{(1 + u')\dot{w}' - (w' + w'_\circ)\dot{u}'}{\lambda^2} \tag{14}$$

Expanding Eq. (14) in a Taylor series, retaining terms up-to order O(ϵ^4), recalling that u and w are evaluated here at the reference axis where ($\zeta = 0$) and using Eq. (9), one can rewrite $\dot{\theta}^2$ as

$$\dot{\theta}^2 = \dot{\bar{w}}'^2 - 2\dot{\bar{w}}'^2\bar{u}' - 2\bar{w}'^2\dot{\bar{w}}'^2 - 4w'_\circ\bar{w}'\dot{\bar{w}}'^2 \tag{15}$$

The strain energy of the beam can be expressed as

$$V = \frac{1}{2}\int_0^{\ell_b}\int_0^{A_b} E\,\varepsilon_{xx}^2\; dA_b\, dx \tag{16}$$

where

$$\begin{aligned}\varepsilon_{xx}^2 =& \bar{u}'^2 + 2w_\circ'\bar{w}'\bar{u}' + w_\circ'^2\bar{w}'^2 + \bar{w}'^2\bar{u}' + w_\circ'\bar{w}'^3 + \frac{1}{4}\bar{w}'^4 \\ &- 2\zeta\bar{w}''\bar{u}' - 2\zeta w_\circ'\bar{w}'\bar{w}'' - \zeta\bar{w}'^2\bar{w}'' + \zeta^2\bar{w}''^2\end{aligned} \tag{17}$$

substituting this equation back into Eq. (16) yields

$$V = \int_0^{\ell_b}\Big[\underbrace{\frac{EA_b}{2}\Big(\bar{u}' + w_\circ'\bar{w}' + \frac{\bar{w}'^2}{2}\Big)^2}_{\mathbf{V_1}} + \underbrace{\frac{EI_b}{2}\bar{w}''^2}_{\mathbf{V_2}}\Big]\,dx \tag{18}$$

The total kinetic energy is the sum of the kinetic energies of the beam mass T_{bm} and rotary inertia T_{br} and the the arms mass T_{am} and rotary inertia T_{ar}

$$T = T_{bm} + T_{br} + T_{am} + T_{ar} \tag{19}$$

The beam kinetic energy can be written as

$$\begin{aligned}T_{bm} + T_{br} &= \frac{1}{2}\int_0^V \rho((\dot{\bar{u}} - \zeta\dot{\bar{w}}')^2 + \dot{\bar{w}}^2)\,dV \\ &= \frac{1}{2}\int_0^V \rho(\dot{\bar{u}}^2 - 2\zeta\dot{\bar{w}}'\dot{\bar{u}} + \zeta^2\dot{\bar{w}}'^2 + \dot{\bar{w}}^2)\,dV \\ &= \frac{1}{2}\int_0^{\ell_b}(\rho A_b(\dot{\bar{u}}^2 + \dot{\bar{w}}^2) + \rho I_b\,\dot{\bar{w}}'^2)\,dx\end{aligned} \tag{20}$$

The translational kinetic energy of the tweezers arms is

$$T_{am} = \frac{1}{2}\int_0^{\ell_b} m_a\,\delta_d\,\dot{\bar{w}}^2\,dx \tag{21}$$

where δ_d is the sum of two Dirac-Delta functions expressed as

$$\delta_d = \delta_{d_1}(x - \ell_1) + \delta_{d_1}(x - \ell_2)$$

The rotary kinetic energy of the arms is

$$T_{ar} = \frac{1}{2}\int_0^{\ell_b} J_a\,\delta_d\,\dot{\theta}^2\,dx \tag{22}$$

where J_a is

$$J_a = \frac{1}{3}m_a\ell_a^2 \tag{23}$$

Using Eq. (15) in Eq. (22), one can write the kinetic energy of the arms rotary inertia as

$$T_{ar} = \frac{1}{2}\int_0^{\ell_b} J_a\,\delta_d\,(\dot{\bar{w}}'^2 - 2\dot{\bar{w}}'^2\bar{u}' - 2\bar{w}'^2\dot{\bar{w}}'^2 - 4w_\circ'\bar{w}'\dot{\bar{w}}'^2)\,dx \tag{24}$$

Therefore, the total kinetic energy of the arch micro-tweezers can be written as

$$\begin{aligned}T = \int_0^{\ell_b}\Big[&\underbrace{\frac{1}{2}\Big(\rho A_b + m_a\delta_d\Big)\dot{\bar{w}}^2}_{\mathbf{T_1}} + \underbrace{\frac{1}{2}\rho A_b\,\dot{\bar{u}}^2}_{\mathbf{T_2}} \\ &+ \underbrace{\frac{1}{2}\Big(\rho I_b + J_a\delta_d(1 - 2\bar{u}' - 2\bar{w}'^2 - 4w_\circ'\bar{w}')\Big)\dot{\bar{w}}'^2}_{\mathbf{T_3}}\Big]\,dx\end{aligned} \tag{25}$$

3.1. Extended hamilton principle

The extended Hamilton principle states that the variation of the summation of the Lagrangian $\mathcal{L} = T - V$ and the line integral of the virtual work done by nonconservative forces W_{nc} during a time interval from t_1 to t_2 must be equal to zero

$$\int_{t_1}^{t_2}\delta\,(T - V + W_{nc})\,dt = 0 \tag{26}$$

where δ is a differential operator denoting the first variation. The first variation of mid-plane potential V_1 in Eq. (18) is obtained as

$$\begin{aligned}&\int_{t_1}^{t_2}\delta V_1\,dt \\ &= \int_{t_1}^{t_2} EA_b\Big(\bar{u}' + w_\circ'\bar{w}' + \frac{\bar{w}'^2}{2}\Big)\delta\bar{u}\,dt\Big|_0^{\ell_b} \\ &- \int_{t_1}^{t_2}\int_0^{\ell_b} EA_b\Big(\bar{u}' + w_\circ'\bar{w}' + \frac{\bar{w}'^2}{2}\Big)'\delta\bar{u}\,dx\,dt \\ &+ \int_{t_1}^{t_2} EA_b\Big(\bar{u}' + w_\circ'\bar{w}' + \frac{\bar{w}'^2}{2}\Big)\bar{w}'\delta\bar{w}\,dt\Big|_0^{\ell_b} \\ &- \int_{t_1}^{t_2}\int_0^{\ell_b} EA_b\Big[\Big(\bar{u}' + w_\circ'\bar{w}' + \frac{\bar{w}'^2}{2}\Big)\bar{w}'\Big]'\delta\bar{w}\,dx\,dt \\ &+ \int_{t_1}^{t_2} EA_b\Big(\bar{u}' + w_\circ'\bar{w}' + \frac{\bar{w}'^2}{2}\Big)w_\circ'\delta\bar{w}\,dt\Big|_0^{\ell_b} \\ &- \int_{t_1}^{t_2}\int_0^{\ell_b} EA_b\Big[\Big(\bar{u}' + w_\circ'\bar{w}' + \frac{\bar{w}'^2}{2}\Big)w_\circ'\Big]'\delta\bar{w}\,dx\,dt\end{aligned} \tag{27}$$

similarly, the first variation of the section bending potential V_2 yields

$$\begin{aligned}&\int_{t_1}^{t_2}\delta V_2\,dt = \int_{t_1}^{t_2}\int_0^{\ell_b} EI_b\,\bar{w}''\delta\bar{w}''\,dx\,dt \\ &+ \int_{t_1}^{t_2}\Big(EI_b\,\bar{w}''\,\delta\bar{w}'\Big|_0^{\ell_b} - EI_b\,\bar{w}'''\,\delta\bar{w}\Big|_0^{\ell_b} + \int_0^{\ell_b} EI_b\,\bar{w}^{iv}\,\delta\bar{w}\,dx\Big)dt \\ &= \int_{t_1}^{t_2} EI_b\,\bar{w}''\,\delta\bar{w}'\,dt\Big|_0^{\ell_b} - \int_{t_1}^{t_2} EI_b\,\bar{w}'''\,\delta\bar{w}\,dt\Big|_0^{\ell_b} \\ &+ \int_{t_1}^{t_2}\int_0^{\ell_b} EI_b\,\bar{w}^{iv}\,\delta\bar{w}\,dx\,dt\end{aligned} \tag{28}$$

The variation of the kinetic energy can be evaluated via integration by parts of individual terms. The first variation of T_1 in Eq. (25) can be written as

$$\begin{aligned}\int_{t_1}^{t_2}\delta T_1\,dt = &\int_0^{\ell_b}(\rho A_b + m_a\sum_{k=1}^{2}\delta_d)\dot{\bar{w}}\,\delta\bar{w}\,dx\Big|_{t_1}^{t_2} \\ &- \int_{t_1}^{t_2}\int_0^{\ell_b}(\rho A_b + m_a\sum_{k=1}^{2}\delta_d)\ddot{\bar{w}}\,\delta\bar{w}\,dx\,dt\end{aligned} \tag{29}$$

similarly the first variation of T_2 is

$$\int_{t_1}^{t_2}\delta T_2\,dt = \int_0^{\ell_b}\rho A_b\,\dot{\bar{u}}\,\delta\bar{u}\,dx\Big|_{t_1}^{t_2} - \int_{t_1}^{t_2}\int_0^{\ell_b}\rho A_b\,\ddot{\bar{u}}\,\delta\bar{u}\,dx\,dt \tag{30}$$

and the first variation of T_3 can be written as

$$\int_{t_1}^{t_2}\delta T_3\,dt = \int_{t_1}^{t_2}\int_0^{\ell_b}\Big(\frac{\partial T_3}{\partial\bar{w}'}\delta\bar{w}' + \frac{\partial T_3}{\partial\bar{u}'}\delta\bar{u}' + \frac{\partial T_3}{\partial\dot{\bar{w}}'}\delta\dot{\bar{w}}'\Big)\,dx\,dt \tag{31}$$

Now, break the variation of Eq. (31) into three individual parts and then perform the integration by parts. The first variation of the first term can be obtained as

$$\begin{aligned}\int_{t_1}^{t_2}\int_0^{\ell_b}\Big(\frac{\partial T_3}{\partial\bar{w}'}\Big)\delta\bar{w}'\,dx\,dt = &\int_{t_1}^{t_2}\gamma_1\,\delta\bar{w}\,dt\Big|_0^{\ell_b} \\ &- \int_{t_1}^{t_2}\int_0^{\ell_b}\gamma_2\,\delta\bar{w}\,dx\,dt\end{aligned} \tag{32}$$

the first variation of the second term gives

$$\begin{aligned}\int_{t_1}^{t_2}\int_0^{\ell_b}\Big(\frac{\partial T_3}{\partial\bar{u}'}\Big)\delta\bar{u}'\,dx\,dt = &\int_{t_1}^{t_2}\gamma_3\,\delta\bar{u}\,dt\Big|_0^{\ell_b} \\ &- \int_{t_1}^{t_2}\int_0^{\ell_b}\gamma_4\,\delta\bar{u}\,dx\,dt\end{aligned} \tag{33}$$

while the first variation of the third term yields

$$\int_{t_1}^{t_2}\int_0^{\ell_b}\left(\frac{\partial T_3}{\partial \dot{\bar{w}}'}\right)\delta\dot{\bar{w}}'\,dx\,dt = \int_0^{\ell_b}\gamma_5\,\delta\bar{w}'\,dx\Big|_{t_1}^{t_2} - \int_{t_1}^{t_2}\gamma_6\,\delta\bar{w}\,dt\Big|_0^{\ell_b} + \int_{t_1}^{t_2}\int_0^{\ell_b}\gamma_7\,\delta\bar{w}\,dx\,dt \tag{34}$$

where the γ_i parameters are listed in Appendix.

The variation of the virtual work due to the electrostatic force, viscous linear damping and nonlinear squeeze-film damping can be written as

$$\int_{t_1}^{t_2}\delta W_{nc}\,dt = \int_{t_1}^{t_2}\left(\int_0^{\ell_b}F_{es}\,\delta\bar{w}\,dx - c_{va}\dot{\bar{u}}\,\delta\bar{u} - (c_{vt}+c_{sf})\dot{\bar{w}}\,\delta\bar{w}\right)dt \tag{35}$$

where F_{es} is the electrostatic force. For parallel-plate model, it can be expressed as

$$F_{PP} = -\frac{1}{2}\frac{\epsilon\, b\, V^2}{(d+w_\circ+\bar{w})^2} \tag{36}$$

The electrostatic force F_{es} can be modified to account for the fringing field by replacing the width of the arch micro-beam b with an effective width b_e considering two models in the literature:

- Palmer's model [23]

$$F_{PM} = -\frac{1}{2}\frac{\epsilon\, b\, V^2}{(d+w_\circ+\bar{w})^2}\left(1+0.65\frac{(d+w_\circ+\bar{w})}{b}\right) \tag{37}$$

- Kimbali's model [24]

$$F_{KM} = -\frac{1}{2}\frac{\epsilon\, b\, V^2}{(d+w_\circ+\bar{w})^2}\left(0.0612+\frac{d^4}{b^4}((d+w_\circ+\bar{w})^2)^2 - 0.5\frac{d^3}{b^3}(d+w_\circ+\bar{w})^2 + 1.5\frac{d^2}{b^2}(d+w_\circ+\bar{w})^2 + 1.2\right) \tag{38}$$

In addition, c_{va} and c_{vt} are the viscous damping coefficients in the axial and transverse directions, respectively. Squeeze-film damping accounts for energy losses due to the narrow channel between the beam and the side electrode. Its damping coefficient c_{sf} can be written as [25]

$$c_{sf} = \frac{\mu\, b^3}{(1+6Kn)(1+w_\circ+\bar{w})^3} \tag{39}$$

where μ is air viscosity, $Kn = \lambda/d$ is Knudsen number and $\lambda = 65$nm is the mean free path of air molecules at ambient pressure.

Substituting Eq. (27)–Eq. (30), Eq. (32)–Eq. (34) into Eq. (26) yields two nonlinear equations of motion describing the system response. The first equation governs the axial response

$$\rho A_b\ddot{\bar{u}} + c_{va}\dot{\bar{u}} + \gamma_4 - EA_b\left(\bar{u}' + w_\circ'\bar{w}' + \frac{\bar{w}'^2}{2}\right)' = 0 \tag{40}$$

the boundary and initial conditions are listed in Appendix. Setting the time derivative terms equal to zero, Eq. (40) reduces to a static equation and can be written as

$$\left(\bar{u}' + w_\circ'\bar{w}' + \frac{\bar{w}'^2}{2}\right)' = 0 \tag{41}$$

The second equation of motion governs the transverse response

$$(\rho A_b + m_a\,\delta_d)\ddot{\bar{w}} - (\rho I_b + J_a\,\delta_d)\ddot{\bar{w}}'' - J_a\,\delta_d'\,\ddot{\bar{w}}' + \gamma_8 + (c_{vt}+c_{sf})\dot{\bar{w}} + EI_b\bar{w}^{iv} - EA_b\left[\left(\bar{u}' + w_\circ'\bar{w}' + \frac{\bar{w}'^2}{2}\right)(w_\circ' + \bar{w}')\right]' = -F_{es} \tag{42}$$

the boundary and initial conditions as well as γ_8 are listed in Appendix.

Equation Eq. (41) can be used to write $\bar{u}$ in terms of $\bar{w}$ by integrating once over x which results in

$$\bar{u}' = -w_\circ'\bar{w}' - \frac{\bar{w}'^2}{2} + c_1 \tag{43}$$

Integrating once more over x and recalling that the axial displacement at both ends is zero ($\bar{u} = 0$) results in

$$\bar{u}(0) = 0 \Rightarrow c_2 = 0 \tag{44a}$$

$$\bar{u}(\ell_b) = 0 \Rightarrow c_1 = \frac{1}{2\ell_b}\int_0^{\ell_b}(2w_\circ'\bar{w}' + \bar{w}'^2)\,dx \tag{44b}$$

Therefore, we can rewrite Eq. (43) as

$$\bar{u}' = -w_\circ'\bar{w}' - \frac{\bar{w}'^2}{2} + \frac{1}{2\ell_b}\int_0^{\ell_b}(2w_\circ'\bar{w}' + \bar{w}'^2)\,dx \tag{45}$$

Substituting with Eq. (45) into Eq. (42) yields

$$(\rho A_b + m_a\,\delta_d)\ddot{\bar{w}} - (\rho I_b + J_a\,\delta_d)\ddot{\bar{w}}'' - J_a\,\delta_d'\,\ddot{\bar{w}}' + \gamma_9 + (c_{vt}+c_{sf})\dot{\bar{w}} + EI_b\bar{w}^{iv} - (w_\circ'' + \bar{w}'')\frac{EA_b}{2\ell_b}\int_0^{\ell_b}(2w_\circ'\bar{w}' + \bar{w}'^2)\,dx = -F_{es} \tag{46}$$

where γ_9 parameter is listed in Appendix. For convenience, we introduce the following nondimensional variables

$$\hat{w} = \frac{\bar{w}}{d},\ \hat{w}_\circ = \frac{w_\circ}{d},\ \hat{x} = \frac{\bar{x}}{l_b},\ t = \frac{\hat{t}}{T},\ \ell_1 = \frac{\hat{\ell}_1}{\ell_b},\ \ell_2 = \frac{\hat{\ell}_2}{\ell_b}$$

where $T = \sqrt{\rho A\ell_b^{\,4}/EI}$ is a time scale. Then, nondimensionalizing the equation of motion, Eq. (46) and multiplying both sides by $\frac{T^2}{d\,\rho A_b}$ results in

$$(1+\alpha_1\,\hat{\delta}_d)\ddot{\hat{w}} - (\alpha_2+\alpha_4\,\hat{\delta}_d)\ddot{\hat{w}}'' - \alpha_4\,\hat{\delta}_d'\,\ddot{\hat{w}}' + \gamma_{10} + (\hat{c}_{vt}+\hat{c}_{sf})\dot{\hat{w}} + \hat{w}^{iv} - \alpha_5(\hat{w}_\circ'' + \hat{w}'')\int_0^1(2\hat{w}_\circ'\hat{w}' + \hat{w}'^2)\,d\hat{x} = -\alpha_6\,F_{es} \tag{47}$$

where

$$\alpha_1 = \frac{m_a}{m_b},\quad \alpha_2 = \frac{I_b}{\ell_b^2 A_b},\quad \alpha_3 = \frac{2}{3}\frac{m_a\,\ell_a^2\,d^2}{m_b\,\ell_b^4}$$
$$\alpha_4 = \frac{2}{3}\frac{m_a\,\ell_a^2}{m_b\,\ell_b^2},\quad \alpha_5 = 6\left(\frac{d}{h_b}\right)^2,\quad \alpha_6 = \frac{6\epsilon\,\ell_b^4}{E\,h^3\,d^3}$$
$$\hat{c}_{vt} = \frac{c_{vt}\,\ell_b^4}{EI_b\,T},\quad \hat{c}_{sf} = \left(\frac{b}{d}\right)^3\frac{T}{m_b}\frac{\mu}{(1+6Kn)(1+\hat{w}_\circ+\hat{w})^3} \tag{48}$$

and γ_{10} is a combination of rotary terms of order $O(\epsilon^3)$ listed in Appendix.

The corresponding nondimensional boundary conditions of the arch micro-beam are

$$w(0,t) = 0,\ w'(0,t) = 0,\ w(1,t) = 0,\ w'(1,t) = 0 \tag{49}$$

On the other hand, if we were to scale the electrostatic gap d at order $O(\epsilon^1)$, similar to the beam width h, the equation of motion would reduce it to a simpler form

$$(1+\alpha_1\,\hat{\delta}_d)\ddot{\hat{w}} - (\alpha_2+\alpha_4\,\hat{\delta}_d)\ddot{\hat{w}}'' - \alpha_4\,\hat{\delta}_d'\,\ddot{\hat{w}}' + (\hat{c}_{vt}+\hat{c}_{sf})\dot{\hat{w}} + \hat{w}^{iv} - \alpha_5(\hat{w}_\circ'' + \hat{w}'')\int_0^1(2\hat{w}_\circ'\hat{w}' + \hat{w}'^2)\,d\hat{x} = -\alpha_6\,F_{es} \tag{50}$$

where the arms rotary inertia terms γ_{10} scale at order $O(\epsilon^5)$ and, therefore, can be neglected.

3.2. Reduced order model

A reduced order model based on a Galerkin approximation is utilized to solve the equation of motion. This technique discretizes the equation of motion in terms of a finite number of degrees-of-freedom describing the amplitude of mode shapes that satisfy the boundary conditions. In this case, we chose to utilize the mode shapes of a straight beam $\phi_i(x)$. Therefore, the solution is assumed as

$$\hat{w}(\hat{x},\hat{t}) = \sum_{i=1}^{N}\phi_i(\hat{x})q_i(\hat{t}) \tag{51}$$

where N is the number of modes retained in the discretization process and $q_i(t)$ are the generalized coordinates. We multiply both sides of

Eq. (47) and Eq. (50) by $(1+\hat{w}_\circ+\hat{w})^2$ to regularize the response near the singularity [26], substitute with Eq. (51), multiply by individual mode shapes ϕ_j and integrate along the beam length to obtain the discretized equations of motion.

We solve for the static deflection of the arch beam $\hat{w}_s(x)$ as a function of Root-Mean-Square RMS V_{RMS} voltage by eliminating the time derivatives from the non-dimensional equations of motion Eq. (47) and Eq. (50) to obtain an identical equilibrium equation in both cases

$$\hat{w}_s^{iv} = \alpha_5\left(\hat{w}_\circ'' + \hat{w}_s''\right)\int_0^1 \left(2\hat{w}_\circ'\hat{w}_s' + \hat{w}_s'^2\right)d\hat{x} - \alpha_6\frac{V_{RMS}^2}{(1+\hat{w}_\circ+\hat{w}_s)^2} \tag{52}$$

subjected to the following boundary conditions

$$\hat{w}_s(0) = 0,\ \hat{w}_s'(0) = 0,\ \hat{w}_s(1) = 0 \text{ and } \hat{w}_s'(1) = 0 \tag{53}$$

The static deflection of the micro-tweezers $\hat{w}_s$ can also be written in terms of a Galerkin approximation as

$$\hat{w}_s(\hat{x}) = \sum_{i=1}^{N}\phi_i(x)q_i(t) \tag{54}$$

Substituting Eq. (54) into Eq. (52), we obtained

$$\begin{aligned}&(1+w_\circ+\sum_{i=1}^{N}\phi_i q_i)^2\left[\sum_{i=1}^{N}\phi_i^{iv}q_i - \alpha_5\left(w_\circ'' + \sum_{i=1}^{N}\phi_i'' q_i\right)\right.\\ &\left.\times\int_0^1\left[\left(\sum_{i=1}^{N}\phi_i' q_i\right)^2 + 2w_\circ'\sum_{i=1}^{N}\phi_i' q_i\right]d\hat{x}\right] + \alpha_6 V_{RMS}^2 = 0\end{aligned} \tag{55}$$

Multiplying this equation by the mode shapes $\phi_j(x)$ and carrying out the integration over the beam length results in N algebraic equations describing the equilibrium position.

Then, the resulting equations can be solved for the generalized coordinates q_i describing available equilibrium positions at a given voltage V_{RMS}. We determined those equilibria and their eigenvalues via a continuation method [27]. Stable equilibria were identified by a set of eigenvalues where all real parts were negative. Unstable equilibria were identified by the presence of one or two eigenvalues with positive real parts.

4. Results and discussion

The fidelity of a ROM depends on the type and number of mode shapes used in the Galerkin expansion [26]. We carried out convergence analysis to determine the minimum number of modes required in the Galerkin expansion by comparing the static response obtained from ROMs employing two, three and five symmetric modes and a parallel-plate electrostatic field model.

Figure Fig. 5 shows the change in the mid-point rise $w_s(0.5)$ as a function RMS voltage for the three ROMs. In all cases, two branches of stable equilibria (marked by solid lines) and two branches of unstable equilibria (marked by dashed lines) are observed. The results show that three modes, at least, are required for model convergence. Using two modes in the model results in quantitative errors along the second branch of stable equilibria and qualitative errors along the second branch of unstable equilibria. Henceforth, we adopt the five-mode ROM in the rest of this work.

The figure also shows that the mid-point rise decreases with increasing RMS voltage along the first branch of stable equilibria, corresponding to the initial beam curvature, until it meets the first branch of unstable equilibria in a saddle-node bifurcation at point S ($V_S = 112.7$ V). This leads to a snap-through, and it jumps-down along the line marked ST, towards the second branch of stable equilibria corresponding to the counter beam curvature.

Decreasing the RMS voltage after snap-through decreases the counter-rise of the mid-point along the second stable branch until it meets the first unstable branch in another saddle-node bifurcation at point B ($V_B = 100.2$ V). As a result, the beam snaps-back, and it jumps-up along the line marked R, towards the first branch of stable equilibria.

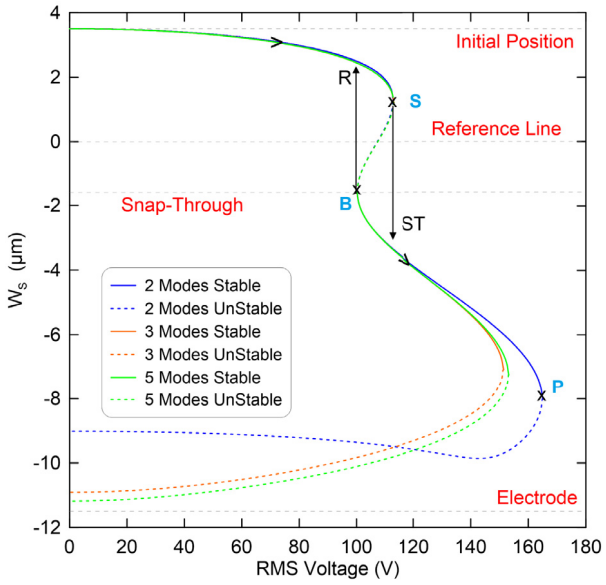

Fig. 5. The beam mid-point rise as a function of RMS voltage from ROMs employing two, three and five symmetric modes in the Galerkin expansion without accounting for the fringing field.

Increasing the voltage beyond the snap-through voltage V_S increases the counter rise of the mid-point along the second stable branch until it reaches a third saddle-node bifurcation demarcating the "pull-in instability" at point P ($V_P = 153.2$ V) where it meets the second branch of unstable equilibria. No equilibria exist beyond the pull-in point. The jump-down and jump-up events at points B and S are used to grasp and release micro-particles. The second stable branch represents the operational range of the tweezers allowing for increased or decreased pressure on object and for the grasping of smaller objects.

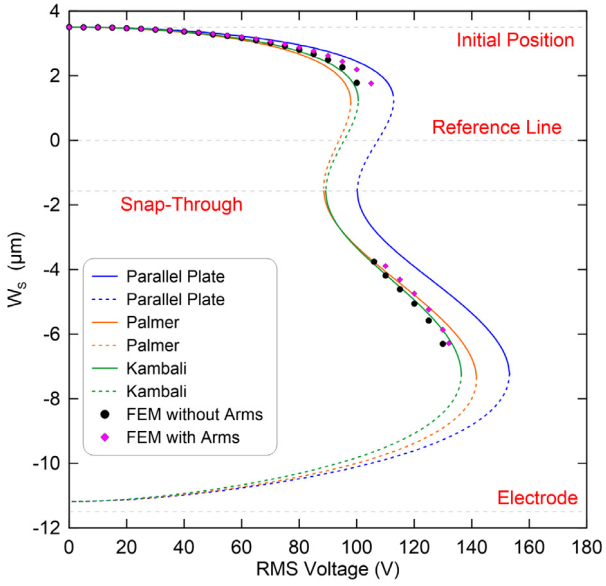

Fig. 6. The beam mid-point rise as a function of RMS voltage using the parallel-plate model (blue line –), Palmer's model (orange line –), Kimbali's model (black line –), FEM without arms (• symbols) and FEM with arms (♦ symbols). (For interpretation of the references to color in this figure legend, the reader is referred to the web version of this article.)

In order to validate the ROM, the FEM package COMSOL Multiphysics (5.3a) [28] was also used to solve for the static response of

the tweezers. A 3D model of the tweezers was created following the dimensions and material properties listed in Table 2. The stationary electrode (1000 × 30 × 3) μm was placed opposite the tweezers and both of them were enclosed in air box (1000 × 100 × 270) μm to represent the electrostatic field. The tweezers was grounded while the electrode voltage was set to V_{RMS}. The boundary conditions fixed the tweezers at its anchors.

Tetrahedral elements were used to mesh the beam, arms, air box and stationary electrode. The total number of elements was 50 359 and their sizes varied in the range 10–80 μm. The Electromechanics module was used to perform the static analysis. Applied voltage was set initially to $V_{RMS} = 0$ and gradually increased in steps of 5 V over a range of [0–150] V to capture the locations of the snap-through and pull-in voltages.

Figure Fig. 6 shows the mid-point rise values calculated by the FEM models with (♦ symbols) and without (• symbols) arms and ROMs employing three electrostatic field models: the traditional parallel-plate model (blue lines) as well as Palmer's (orange lines) and Kimbali's (green lines) models accounting for the fringing field. Comparing the results of the FEM without arms and the parallel-plate ROM shows that ignoring the fringing field underestimates the electrostatic force and overestimates the saddle–node bifurcation points. The ROMs accounting for the fringing field compare well with the FEM without arms. Henceforth, we adopt Kimbali's model because it better matches the FEM results. Further, comparing the two FEMs shows that introducing the arms increases the voltage required for snap-through from 106 V to 110 V. On the other hand, the arms do not result in a significant change along the second stable branch.

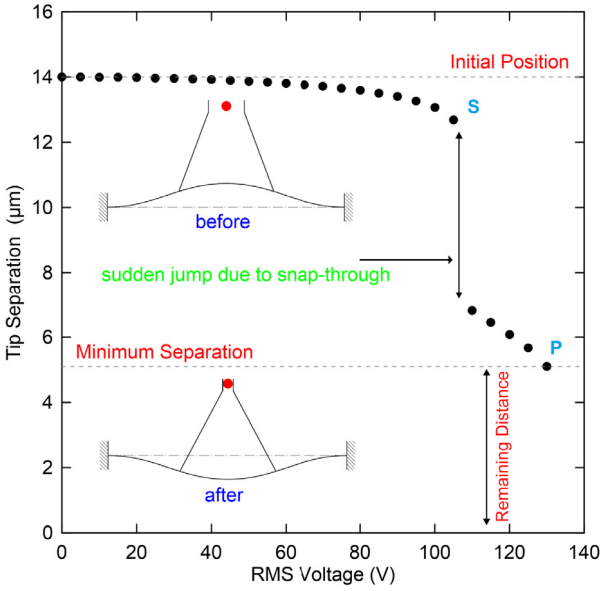

Fig. 7. The tip separation as a function of the RMS voltage calculated using FEM.

The FEM was also used to calculate the arm tips' separation as a function of RMS voltage as shown in Fig. 7. At 0 V, the separation distance is 14 μm, corresponding to the initial distance. The distance decreases as the voltage increases and the beam rise follows the first branch of stable equilibria until snap-down at $V_S = 110$ V. As a result, the separation distance drops from 12.66 μm to 7.18 μm.

Schematic drawings the tweezers before and after snap-through are shown in top and bottom insets of the figure. Increasing the RMS voltage further, reduces the distance to 5.1 μm at 130 V. Pull-in occurs at a higher voltage not captured by the large voltage step in this FEM simulation. We note that the separation distance varies smoothly along the second stable branch demonstrating the tweezers ability to smoothly grasp, manipulate and compress objects. The arms

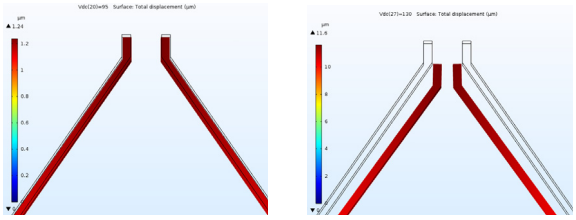

(a) 95V (b) 130V

Fig. 8. A snapshot of the tweezers (a) before $V_{RMS} = 95$ V and (b) after $V_{RMS} = 130$ V snap-through.

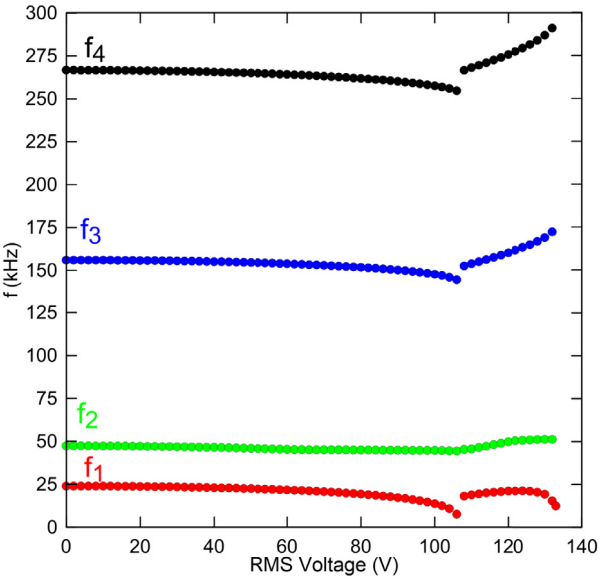

Fig. 9. Variation of the tweezers' first four natural frequencies with RMS voltage.

configuration along the first stable branch ($V_{RMS} = 95$ V) and the second stable branch ($V_{RMS} = 130$ V) are shown in Fig. 8.

To examine the stability characteristics of the tweezers along the two stable branches, we used the FEM model with arms to evaluate the first four natural frequencies around these equilibria. The model followed the two branches in steps of 2 V. The results are shown in Fig. 9. The first natural frequency f_1, corresponding to the first symmetric mode Fig. 10 (a), drops continuously along the first stable branch (initial curvature) to reach zero at snap-through voltage $V_S = 110$ V. The first natural frequency f_1 along the second branch (counter curvature) is $f_1 = 23.5$ kHz after snap-through. As the voltage increases, the natural frequency f_1 drops to reach zero at pull-in voltage V_P.

The second natural frequency, corresponding to the first asymmetric mode Fig. 10 (b), varies continuously with voltage within a small range. It does not evince a discontinuity as the equilibrium position jumps from the first to the second stable branch at snap-through. The third and fourth natural frequencies, corresponding to the second symmetric and asymmetric modes Fig. 10 (c) and (d), respectively, also vary within a small range with voltage. However, they evince jumps to higher values after snap-through. The relatively large fundamental natural frequency and the narrow variation range of the natural frequencies with voltage indicate that the tweezers is stable against parameter disturbance except in the immediate vicinity of snap-through and pull-in.

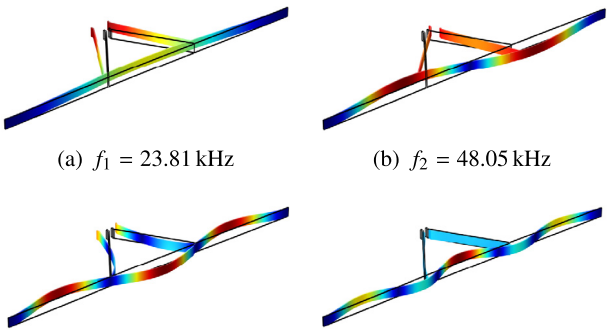

(a) $f_1 = 23.81$ kHz (b) $f_2 = 48.05$ kHz

(c) $f_3 = 155.35$ kHz (d) $f_4 = 264.94$ kHz

Fig. 10. The first four mode shapes of the tweezers at $V_{RMS} = 0$.

The first four in-plane bending mode shapes of the tweezers at $V_{RMS} = 0$ were found to be the first symmetric, Fig. 10 (a), the first asymmetric, Fig. 10 (b), the second symmetric, Fig. 10 (c), and the second asymmetric, Fig. 10 (d), mode shapes. The arms motions were in-phase in the first and second modes and out-of-phase in the third and fourth modes.

5. Conclusion

In this paper, we presented a novel electrostatic micro-tweezers consisting of two arms mounted to an initially curved beam. The grip mechanism uses the bistability of initially curved beams to close the distance between the arm tips. It can capture hard micro-particles, such as polystyrene beads, or soft micro objects, such as cells in aqueous media [5,29,30]. A model accounting for the effects of tweezers arms inertia, the arch beam mid-plane strteching and rotary inertia, and the electrostatic fringing field was developed. A reduced-order model was developed to represent the tweezers taking into account the arms' inertia and the electrostatic fringing field. An FEM model was also developed to validate the ROM. Simulation results show that small differences between the ROM and FEM models of the tweezers in the vicinity of snap-through and negligible differences elsewhere. The results also show that ability of the tweezers to manipulate micro-particles in the range of 5–12 μm and to smoothly compress and hold objects along the second stable branch, corresponding to operating voltage range from snap-back $V_B = 100.2$ V to pull-in $V_P = 153.2$ V. Finally, the arch micro-tweezers were fabricated using SOI process.

In future wrok, we will compare the results of the tweezers model accouting for higher order rotary inertia terms Eq. (47) with that neglecting them Eq. (50) to examine the validity of the assumption underlying the latter. We will also study the dynamic response of the micro-tweezers analytically and experimentally.

Acknowledgments

The authors would like to acknowledge Canadian Microsystems Corporation provision of products and services that facilitated this research. The first author acknowledges the support of Jazan University and the second author acknowledges support of KFUPM.

Appendix

$$
\begin{aligned}
\gamma_1 &= -2J_a\,\delta_d\,\dot{\bar{w}}'^2(\bar{w}' + w_\circ') \\
\gamma_2 &= -2J_a\,\delta_d'\,\dot{\bar{w}}'^2(\bar{w}' + w_\circ') - J_a\,\delta_d\,\left(2\dot{\bar{w}}'^2(\bar{w}'' + w_\circ'') + 4\dot{\bar{w}}''(\bar{w}' + w_\circ')\right) \\
\gamma_3 &= -J_a\,\delta_d\,\dot{\bar{w}}'^2 \\
\gamma_4 &= -J_a\,\delta_d'\,\dot{\bar{w}}'^2 - 2J_a\,\delta_d\,\dot{\bar{w}}'\dot{\bar{w}}'' \\
\gamma_5 &= (\rho I_b + J_a\,\delta_d)\ddot{\bar{w}}' - 2J_a\,\delta_d\dot{\bar{w}}'(\bar{u}' + \bar{w}'^2 + 2w_\circ'\bar{w}') \\
\gamma_6 &= (\rho I_b + J_a\,\delta_d)\ddot{\bar{w}}' - J_a\,\delta_d\,\left(4\dot{\bar{w}}'^2(\bar{w}' + w_\circ') + 2\ddot{\bar{w}}'(\bar{u}' + \bar{w}'^2 + 2w_\circ'\bar{w}')\right) \\
\gamma_7 &= (\rho I_b + J_a\,\delta_d)\ddot{\bar{w}}'' - J_a\,\delta_d'\,\Big(4\ddot{\bar{w}}'^2(\bar{w}' + w_\circ') + 2\ddot{\bar{w}}'(-\tfrac{1}{2} + \bar{u}' + \bar{w}'^2 \\
&\quad + 2w_\circ'\bar{w}')\Big) - J_a\,\delta_d\,\Big(2\ddot{\bar{w}}'(\bar{u}'' + 2\bar{w}'\bar{w}'' + 2w_\circ''\bar{w}' + 2w_\circ'\bar{w}'') \\
&\quad + 8\dot{\bar{w}}''(\bar{w}'\dot{\bar{w}}' + w_\circ'\dot{\bar{w}}') + 4\dot{\bar{w}}'^2(\bar{w}'' + w_\circ'') + 2\ddot{\bar{w}}''(\bar{u}' + \bar{w}'^2 + 2w_\circ'\bar{w}')\Big) \\
\gamma_8 &= -J_a\,\delta_d'\,\left(2\dot{\bar{w}}'^2(\bar{w}' + w_\circ') + 2\ddot{\bar{w}}'(\bar{u}' + \bar{w}'^2 + 2w_\circ'\bar{w}')\right) \\
&\quad - J_a\,\delta_d\,\Big(2\ddot{\bar{w}}'(\bar{u}'' + 2\bar{w}'\bar{w}'' + 2w_\circ''\bar{w}' + 2w_\circ'\bar{w}'') \\
&\quad + 4\dot{\bar{w}}''(\bar{w}'\dot{\bar{w}}' + w_\circ'\dot{\bar{w}}') + 2\dot{\bar{w}}'^2(\bar{w}'' + w_\circ'') + 2\ddot{\bar{w}}''(\bar{u}' + \bar{w}'^2 + 2w_\circ'\bar{w}')\Big) \\
\gamma_9 &= J_a\,\delta_d'\,\Big(4\bar{w}'\dot{\bar{w}}'^2 + \frac{2\ddot{\bar{w}}'}{\ell_b}\int_0^{\ell_b}(2w_\circ'\bar{w}' + \bar{w}'^2)dx + 2\bar{w}'^2\ddot{\bar{w}}' + 4w_\circ'\dot{\bar{w}}'^2 \\
&\quad + 4w_\circ'\bar{w}'\ddot{\bar{w}}'\Big) + J_a\,\delta_d\,\Big(4\bar{w}''\dot{\bar{w}}'^2 + 4\bar{w}'\dot{\bar{w}}'\bar{w}'' + 8\bar{w}'\dot{\bar{w}}'\dot{\bar{w}}'' \\
&\quad + \frac{2\ddot{\bar{w}}''}{\ell_b}\int_0^{\ell_b}(2w_\circ'\bar{w}' + \bar{w}'^2)dx + 2\bar{w}'^2\ddot{\bar{w}}'' + 4w_\circ''\dot{\bar{w}}'^2 + 4w_\circ''\bar{w}'\ddot{\bar{w}}' \\
&\quad + 4w_\circ'\ddot{\bar{w}}'\bar{w}'' + 8w_\circ'\dot{\bar{w}}'\dot{\bar{w}}'' + 4w_\circ'\bar{w}'\ddot{\bar{w}}'' + 8w_\circ'w_\circ''\ddot{\bar{w}}'\Big) \\
\gamma_{10} &= \alpha_3\hat{\delta}_d'\,\Big(2\hat{w}'\dot{\hat{w}}'^2 + \ddot{\hat{w}}'\int_0^1(2\hat{w}_\circ'\hat{w}' + \hat{w}'^2)d\hat{x} + \hat{w}'^2\ddot{\hat{w}}' + 2\hat{w}_\circ'\dot{\hat{w}}'^2 \\
&\quad + 2\hat{w}_\circ'\hat{w}'\ddot{\hat{w}}'\Big) + \alpha_3\hat{\delta}_d\,\Big(2\hat{w}''\dot{\hat{w}}'^2 + 2\hat{w}'\ddot{\hat{w}}'\hat{w}'' + 4\hat{w}'\dot{\hat{w}}'\dot{\hat{w}}'' \\
&\quad + \ddot{\hat{w}}''\int_0^1(2\hat{w}_\circ'\hat{w}' + \hat{w}'^2)d\hat{x} + \hat{w}'^2\ddot{\hat{w}}'' + 2\hat{w}_\circ''\dot{\hat{w}}'^2 + 2\hat{w}_\circ''\hat{w}'\ddot{\hat{w}}' \\
&\quad + 2\hat{w}_\circ'\ddot{\hat{w}}'\hat{w}'' + 4\,\hat{w}_\circ'\dot{\hat{w}}'\dot{\hat{w}}'' + 2\hat{w}_\circ'\hat{w}'\ddot{\hat{w}}'' + 4\hat{w}_\circ'\hat{w}_\circ''\ddot{\hat{w}}'\Big)
\end{aligned}
\tag{A.1}
$$

The boundary and initial conditions of Eq. (40)

$$
\begin{aligned}
\bar{u}' + w_\circ'\bar{w}' + \frac{\bar{w}'^2}{2} = 0 \text{ or } \bar{u} = 0 \text{ at } x = 0 \;\&\; \ell_b \\
\dot{\bar{u}} = 0 \text{ or } \bar{u} = 0 \text{ at } t_2 = 0
\end{aligned}
\tag{A.2}
$$

The boundary and initial conditions of Eq. (42)

$$
\begin{aligned}
\bar{w}''' - (\bar{u}' + w_\circ'\bar{w}' + \frac{\bar{w}'^2}{2})(w_\circ' + \bar{w}') = 0 \text{ or } \bar{w} = 0 \text{ at } x = 0 \;\&\; \ell_b \\
\bar{w}'' = 0 \text{ or } \bar{w}' = 0 \text{ at } x = 0 \;\&\; \ell_b \\
\dot{\bar{w}} = 0 \text{ or } \bar{w} = 0 \text{ at } t_2 = 0
\end{aligned}
\tag{A.3}
$$

The boundary conditions of the arch beam are given by

$$
\bar{w} = 0 \text{ or } \bar{w}' = 0 \text{ at } x = 0 \;\&\; \ell_b \tag{A.4}
$$

References

[1] Y. Jia, Q. Xu, MEMS microgripper actuators and sensors: The state-of-the-art survey, Recent Pat. Mech. Eng. 6 (2) (2013) 132–142.
[2] S. Yang, Q. Xu, A review on actuation and sensing techniques for MEMS-based microgrippers, J. Micro-Bio Robot. 13 (1–4) (2017) 1–14.
[3] D.-H. Kim, M.G. Lee, B. Kim, Y. Sun, A superelastic alloy microgripper with embedded electromagnetic actuators and piezoelectric force sensors: a numerical and experimental study, Smart Mater. Struct. 14 (6) (2005) 1265.
[4] S. Jericho, M. Jericho, T. Hubbard, M. Kujath, Micro-electro-mechanical systems microtweezers for the manipulation of bacteria and small particles, Rev. Sci. Instrum. 75 (5) (2004) 1280–1282.
[5] F. Beyeler, D.J. Bell, B.J. Nelson, Y. Sun, A. Neild, S. Oberti, J. Dual, Design of a micro-gripper and an ultrasonic manipulator for handling micron sized objects, in: Intelligent Robots and Systems, 2006 Ieee/RSJ International Conference on Intelligent Robots and System, IEEE, 2006, pp. 772–777.

[6] J. Varona, E. Saenz, S. Fiscal-Woodhouse, A. Hamoui, Design and fabrication of a novel microgripper based on electrostatic actuation, in: 52nd IEEE International Midwest Symposium on Circuits and Systems, IEEE, 2009, pp. 827–832.
[7] J. Chang, B.-K. Min, J. Kim, S.-J. Lee, L. Lin, Electrostatically actuated carbon nanowire nanotweezers, Smart Mater. Struct. 18 (6) (2009) 065017.
[8] B. Volland, H. Heerlein, I. Rangelow, Electrostatically driven microgripper, Microelectron. Eng. 61 (2002) 1015–1023.
[9] F. Beyeler, A. Neild, S. Oberti, D.J. Bell, Y. Sun, J. Dual, B.J. Nelson, Monolithically fabricated microgripper with integrated force sensor for manipulating micro objects and biological cells aligned in an ultrasonic field, J. Microelectromech. Syst. 16 (1) (2007) 7–15.
[10] T. Chen, L. Sun, L. Chen, W. Rong, X. Li, A hybrid-type electrostatically driven microgripper with an integrated vacuum tool, Sensors Actuators A 158 (2) (2010) 320–327.
[11] S.A. Bazaz, F. Khan, R.I. Shakoor, Design, simulation and testing of electrostatic SOI MUMPs based microgripper integrated with capacitive contact sensor, Sensors Actuators A 167 (1) (2011) 44–53.
[12] M. Hamedi, P. Salimi, M. Vismeh, Simulation and experimental investigation of a novel electrostatic microgripper system, Microelectron. Eng. 98 (2012) 467–471.
[13] Q. Xu, Design, fabrication and testing of an MEMS microgripper with dual-axis force sensor, IEEE Sens. J. 15 (10) (2015) 6017–6026.
[14] B.K. Chen, Y. Zhang, Y. Sun, Active release of microobjects using a MEMS microgripper to overcome adhesion forces, J. Microelectromech. Syst. 18 (3) (2009) 652–659.
[15] H. Demaghsi, H. Mirzajani, H.B. Ghavifekr, A novel electrostatic based microgripper (cellgripper) integrated with contact sensor and equipped with vibrating system to release particles actively, Microsyst. Technol. 20 (12) (2014) 2191–2202.
[16] H. Chang, H. Zhao, F. Ye, G. Yuan, J. Xie, M. Kraft, W. Yuan, A rotary comb-actuated microgripper with a large displacement range, Microsyst. Technol. 20 (1) (2014) 119–126.
[17] B. Piriyanont, A.G. Fowler, S.R. Moheimani, Force-controlled MEMS rotary microgripper, J. Microelectromech. Syst. 24 (4) (2015) 1164–1172.
[18] S. Krylov, B.R. Ilic, D. Schreiber, S. Seretensky, H. Craighead, The pull-in behavior of electrostatically actuated bistable microstructures, J. Micromech. Microeng. 18 (5) (2008) 055026.
[19] H.M. Ouakad, M.I. Younis, On using the dynamic snap-through motion of MEMS initially curved microbeams for filtering applications, J. Sound Vib. 333 (2) (2014) 555–568.
[20] M. Hafiz, L. Kosuru, A. Ramini, K. Chappanda, M. Younis, In-plane MEMS shallow arch beam for mechanical memory, Micromachines 7 (10) (2016) 191.
[21] W. Lacarbonara, A Theoretical and Experimental Investigation of Nonlinear Vibrations of Buckled Beams (Ph.D. thesis), Virginia Tech, 1997.
[22] S.A. Emam, A Theoretical and Experimental Study of Nonlinear Dynamics of Buckled Beams (Ph.D. thesis), Virginia Tech, 2002.
[23] P.M. Osterberg, S.D. Senturia, M-TEST: a test chip for MEMS material property measurement using electrostatically actuated test structures, J. Microelectromech. Syst. 6 (2) (1997) 107–118.
[24] P.N. Kambali, A.K. Pandey, Capacitance and force computation due to direct and fringing effects in MEMS/NEMS arrays, IEEE Sens. J. 16 (2) (2016) 375–382.
[25] S. Krylov, Lyapunov exponents as a criterion for the dynamic pull-in instability of electrostatically actuated microstructures, Int. J. Non-Linear Mech. 42 (4) (2007) 626–642.
[26] M.I. Younis, E.M. Abdel-Rahman, A. Nayfeh, A reduced-order model for electrically actuated microbeam-based MEMS, J. Microelectromech. Syst. 12 (5) (2003) 672–680.
[27] E.M. Abdel-Rahman, M.I. Younis, A.H. Nayfeh, Characterization of the mechanical behavior of an electrically actuated microbeam, J. Micromech. Microeng. 12 (6) (2002) 759.
[28] COMSOL Multiphysics V. 5.3a. www.comsol.com. COMSOL AB, Stockholm, Sweden.
[29] C. Yamahata, D. Collard, B. Legrand, T. Takekawa, M. Kumemura, G. Hashiguchi, H. Fujita, Silicon nanotweezers with subnanometer resolution for the micromanipulation of biomolecules, J. Microelectromech. Syst. 17 (3) (2008) 623–631.
[30] M. Kumemura, D. Collard, N. Sakaki, C. Yamahata, M. Hosogi, G. Hashiguchi, H. Fujita, Single-DNA-molecule trapping with silicon nanotweezers using pulsed dielectrophoresis, J. Micromech. Microeng. 21 (5) (2011) 054020.